INVERSE PHYSICS-BASED MODELING OF THE 2016 MW 6.1 TOTTORI EARTHQUAKE

Sharing not permitted

This presentation participates in OSPP

Outstanding Student & PhD candidate Presentation contest

LinkedIn

OSPP contest

Martin Hronek[1], martin.hronek493@student.cuni.cz , **František Gallovič**[1], frantisek.gallovic@matfyz.cuni.cz

[1]Department of Geophysics, Faculty of Mathematics and Physics, Charles University, Prague, Czech Republic

CHARLES UNIVERSITY
Faculty of mathematics and physics

1) Background

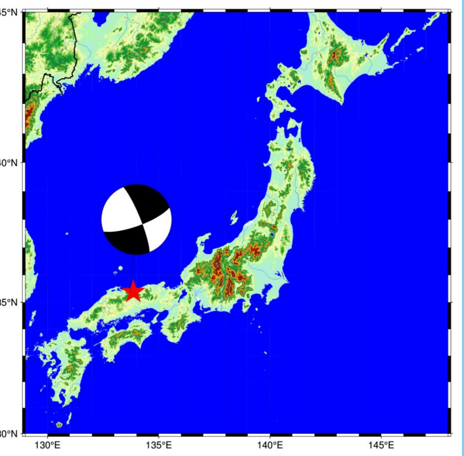

- The 2016 Mw 6.1 shallow crustal left-lateral strike-slip Tottori earthquake occurred in the central part of the Tottori prefecture in the Chugoku region in western Japan.
- It caused strong ground motions with a maximum PGA of 1.4 gal.
- The mainshock was preceded by 70 foreshocks over a 12-hour period (the largest with Mw 4.2) and followed by more than 10,000 aftershocks over the following 10 days (the largest with Mw 5.0).
- This earthquake occurred in the San-in shear zone, which is part of the largest right-lateral Northern Chugoku shear zone.
- The Tottori prefecture has been struck by several large crustal earthquakes with severe damage during the last decade (the 1947 Mw 7.0 Tottori, the 1983 Mw 5.5 Central Tottori, the 2000 Mw 6.7 Western Tottori).

2) Motivation

- Published kinematic rupture models inferred either from geodetic or seismic data exhibit significant discrepancies (Ross et al., 2018; Kubo et al., 2017; Meneses-Gutierrez et al., 2019; Amey et al., 2019; Shibata et al., 2025).
- In this study, we perform a so-far missing dynamic source inversion with slip-weakening friction law with spatially heterogeneous prestress and friction parameters distribution on the fault to better understand this event.

3) Data

- We use data from 21 seismic stations located within 50 km of the epicenter, obtained from the NIED strong-motion seismograph network.
- The data are integrated to velocities and band-pass filtered between 0.05-1.2 Hz (TTR005), 0.1-0.6 Hz (TTRH07) and 0.05-0.6 Hz (others).
- We use horizontal and vertical coseismic static displacements from 33 GNSS Earth Observation Network stations inferred by Meneses-Gutierrez et al. (2019) and Amey et al. (2019).
- 1D layered Crustal model is extrapolated from the Japan Integrated Velocity Structure Model (Koketsu et al., 2008, 2012) under each station separately.
- Location of foreshocks and aftershocks are adopted from Ross et al. (2018).

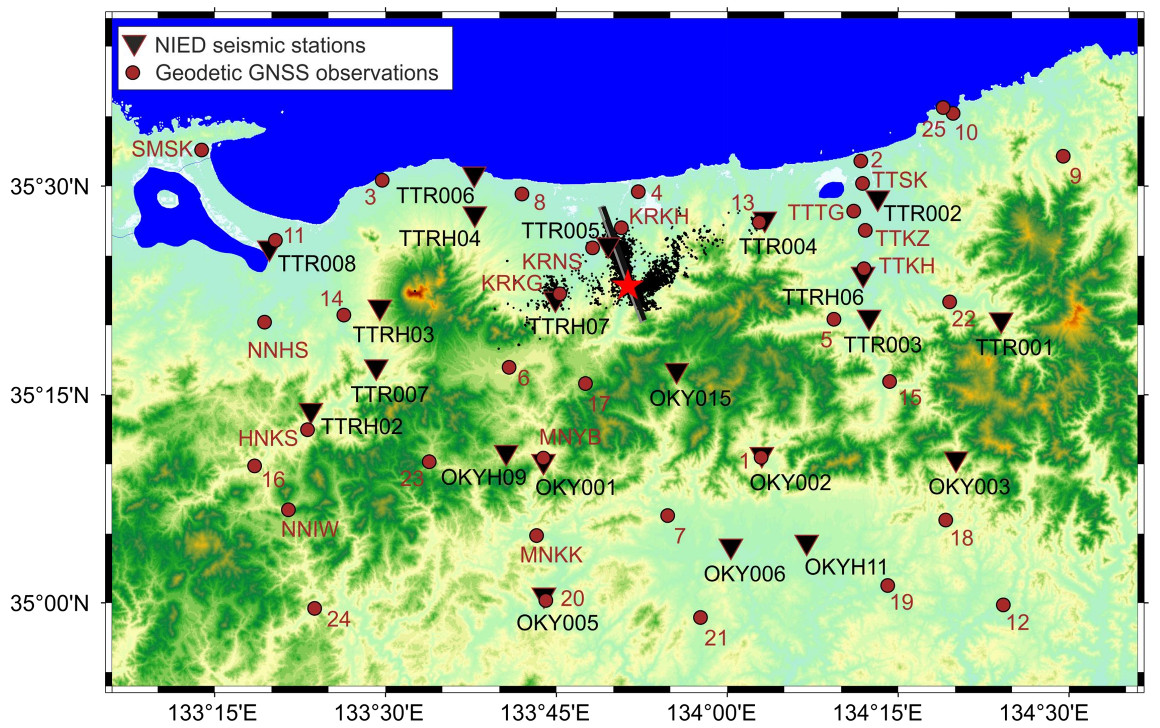

Figure 2: Map of NIED seismic stations (triangles) and geodetic GNSS observations (circles, DPRI marked with their name and GSI marked with numbers) used in this work. The black and gray lines represent the surface projections of the upper and lower along-strike sections of the fault, respectively. The red star indicates the location of the hypocenter, whereas the black dots denote the positions of foreshocks and aftershocks.

4) Method

- We utilize fd3d_tsn_pt code (Gallovič et al., 2020) for dynamic simulation of rupture propagation, calculation of synthetic seismograms and static displacements, and inversion.
- **Forward problem:**
  - We utilize the 3D finite-difference staggered grid code FD3D_TSN (Premus et al., 2020) with GPU acceleration to simulate the dynamic rupture propagation.
  - We assume the classic linear slip-weakening friction law with spatially variable dynamic parameters on a planar vertical fault.
  - Green's functions are precalculated in 1D velocity models acquired for each station from a 3D model (seismic: Axitra code by Cotton and Coutant, 1997; geodetic: Okada, 1985).
  - The result of dynamic simulation is a spatio-temporal distribution of slip rates along the fault.
  - Synthetic seismograms are calculated using the representation theorem (Aki & Richards, 2002).
- **Parameterization :**
  - For forward problem, we prescribe inhomogeneous distributions of the three dynamic parameters of the linear slip-weakening friction law on the fault.
  - Dynamic parameters are *prestress* $T_0 = T_i - T_d$ (i.e. the difference between the initial and dynamic value of the shear traction), *friction drop* $\Delta\mu$ (i.e. the difference between the static and dynamic friction coefficient) and *slip-weakening distance* D_c.
- **Inverse problem:**
  - The inverse problem is formulated in a Bayesian framework, employing the Parallel Tempering Markov Chains Monte Carlo approach to sample the posterior distribution of the model parameters (Sambridge, 2013) with modified Metropolis-Hastings acceptance rule.
  - We assume uniform prior PDFs of the model parameters within wide ranges; see Table 1.
  - We explore the model space using 7 MPI processes on three Nvidia RTX 3070 GPUs, running the computation for a total of 82 days.

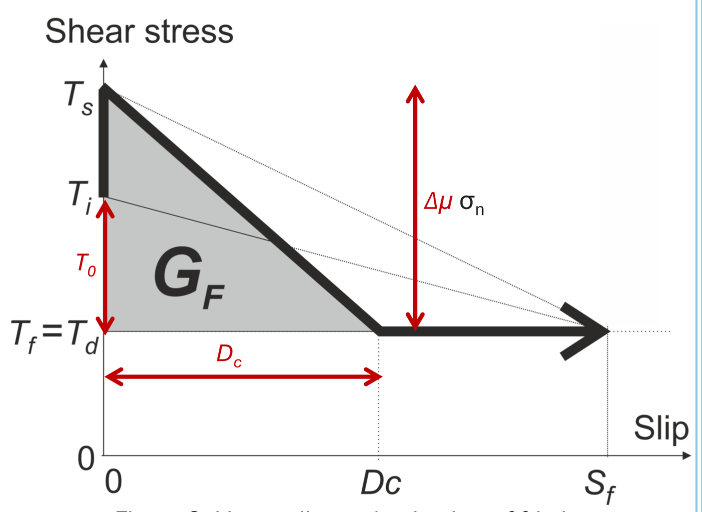

Figure 3: Linear slip-weakening law of friction as a function of shear traction on slip.

Parameter	Value
General	
Fault dimension	Length 16 km, width 16 km
Fault mechanism	Strike 160°, dip 88°, rake 0°
FD3D	
Spatial discretization	100 m
FD half-domain size (along strike, normal, dip)	161, 110, 161
Number of time step (FD)	5 000
Time step in seconds (FD)	2 ms
Dip	90°
Computational time (GPU)	15 s
Green's functions	
Spatial fault discretization	1 km
Maximum computed frequency	2.5 Hz (Nyquist)
Time sampling	0.2 s
Prior ranges of parameters for inversion	
Number of model parameters (discretization)	11, 11
Prestress prior	(0;100) MPa
Static-Dynamic friction coefficient prior	(0; 1.0)
Characteristic slip-weakening distance prior	(0.04; 2.0) m
Nucleation position (along strike, along dip)	11 km, 4.5 km
Nucleation radius prior	1000 m
Data and modeling errors	
Seismic data uncertainty	0.05 m
Mw	(6.05; 6.25)

Table 1: Parameters for forward FD simulation, Green's functions and dynamic inversion model setup.

5) Results

- The total number of visited models is approximately 1.2 million. After the removal of the burn-in phase models, the ensemble used for further analysis consists of 14,764 models.
- Here, we first present the maximum a posteriori (MAP) model, followed by the ensemble with its statistics.

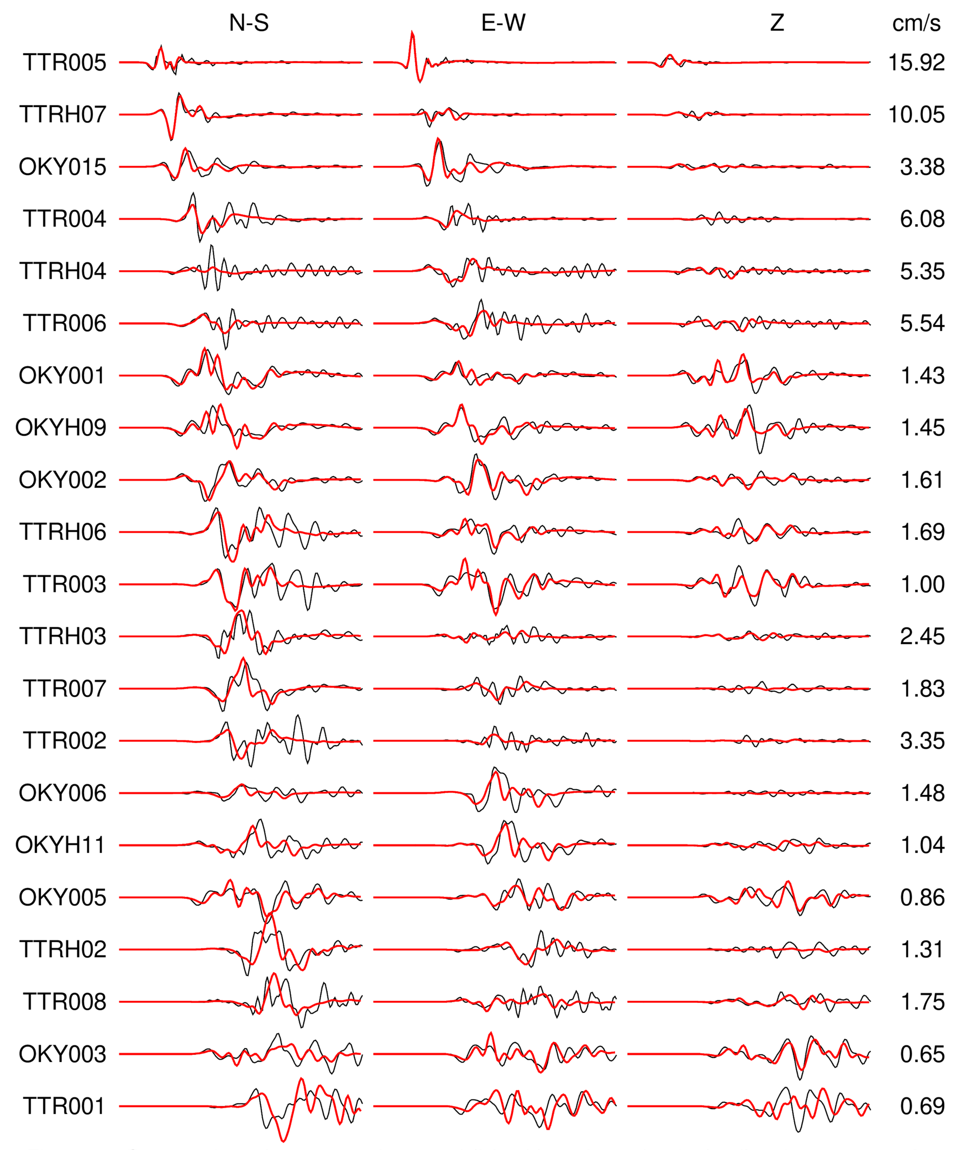

Figure 4: Comparison between observed (black) and synthetic (red) seismograms for the MAP rupture model. The left column lists the seismic station codes, followed by the three components: north-south, east-west, and vertical. The right column displays the amplitudes in cm/s.

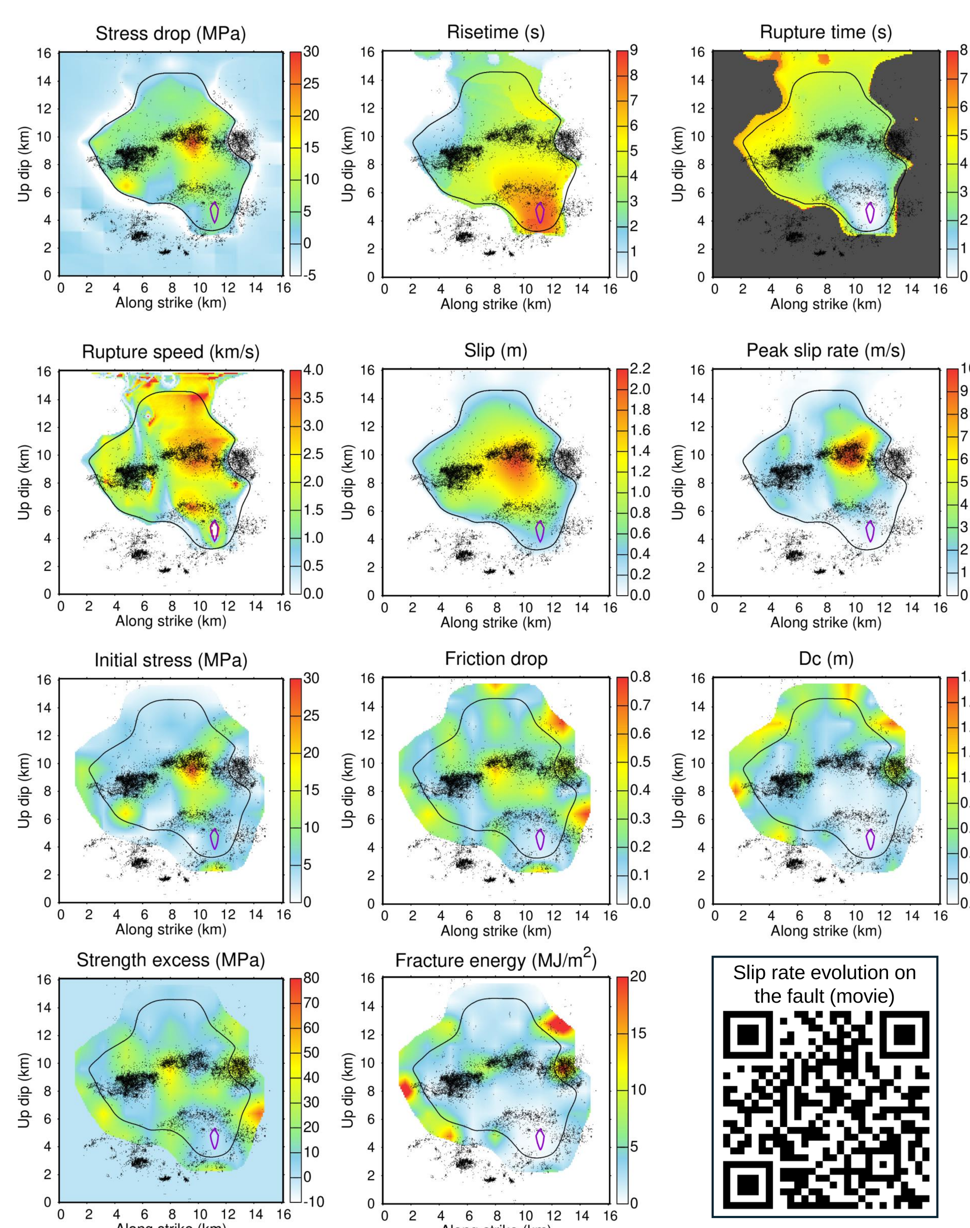

Figure 5: Distribution of the rupture parameters on the fault of the MAP rupture model. Black lines contour the region where the slip exceeds 10% of the maximum slip value, violet line bounds the nucleation and black dots denote foreshocks and aftershocks projected on the fault plane.

Parameter	Value
Ruptured area A_R	$92.76\,\mathrm{km}^2$
Average speed $\overline{v_R}$	$2\,059\,\mathrm{m/s}$
Seismic moment M_0	$2.34 \times 10^{18}\,\mathrm{Nm}$
Average stress drop $\overline{\Delta T}$	$7.75\,\mathrm{MPa}$
Fracture energy E_F	$2.55 \times 10^{14}\,\mathrm{J}$
Radiated energy E_R	$4.01 \times 10^{13}\,\mathrm{J}$
Radiation efficiency η_{rad}	$13.6\,\%$
Seismic misfit	43.69
Seismic VR	54.99 % for shift 0.2 s
GPS misfit	2.31
GPS VR	98.94 %

Table 2: Parameter values for the maximum a posteriori model.

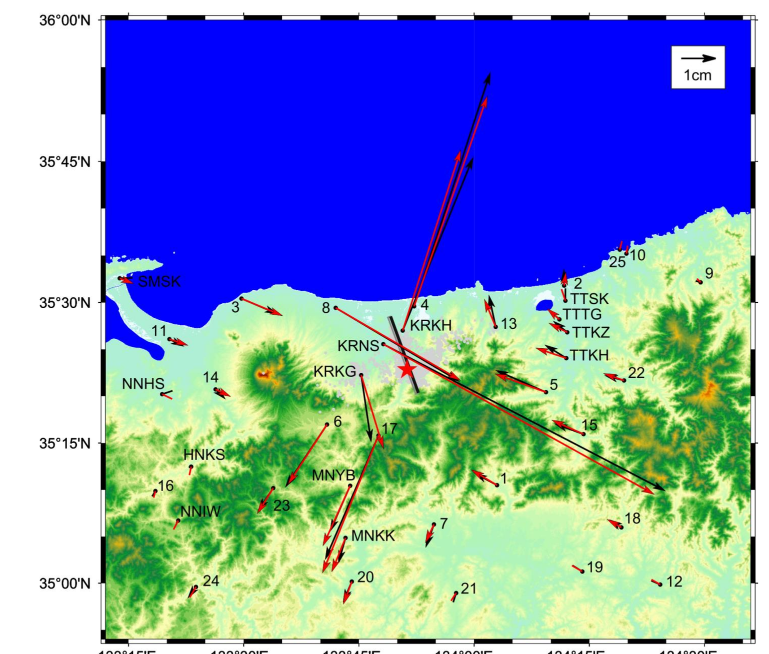

Figure 6: Observed (black) and synthetic (red) GNSS static displacements (scaled) for the MAP rupture model. The thick black and gray lines represent the surface projection of the lower and upper along strike parts of the fault, the red star marks the epicenter location, and the gray dots indicate the positions of foreshocks and aftershocks.

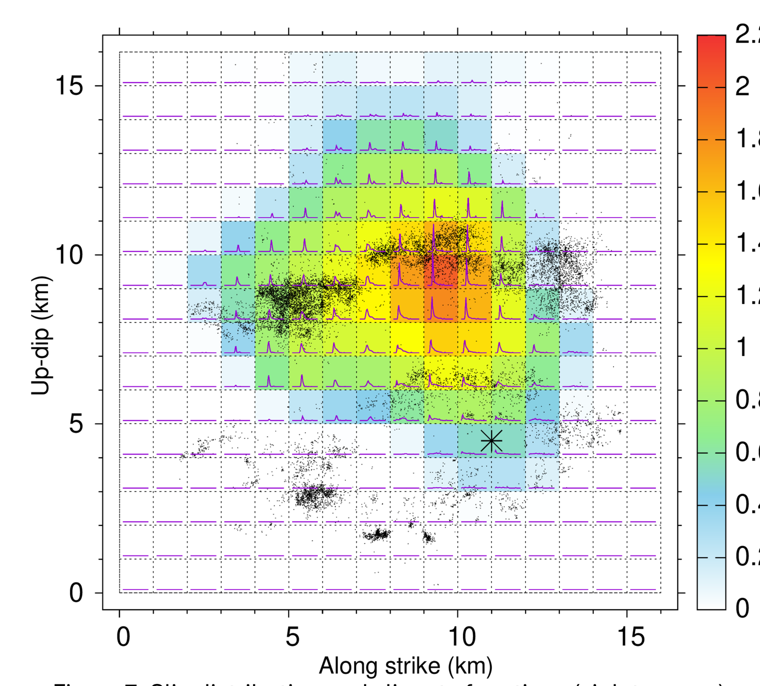

Figure 7: Slip distribution and slip rate functions (violet curves) on the fault (averaged over 1km x 1km subfaults). Black star denotes the position of hypocenter and black dots are foreshocks and aftershocks projected on the fault plane.

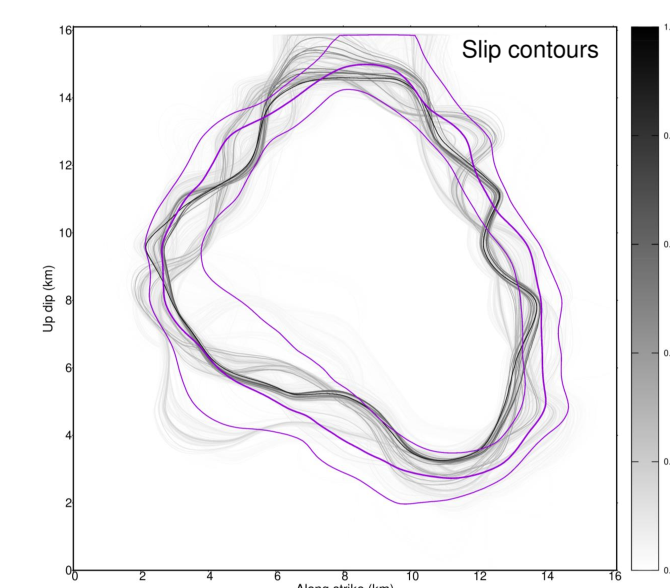

Figure 8: Slip contours on the fault for all accepted model samples. The white-and-black scale represents the normalized probability density function (PDF). Thick violet lines indicate the contours of the mean model, while the two thin violet lines represent the averaged slip model with added and subtracted one-sigma uncertainty.

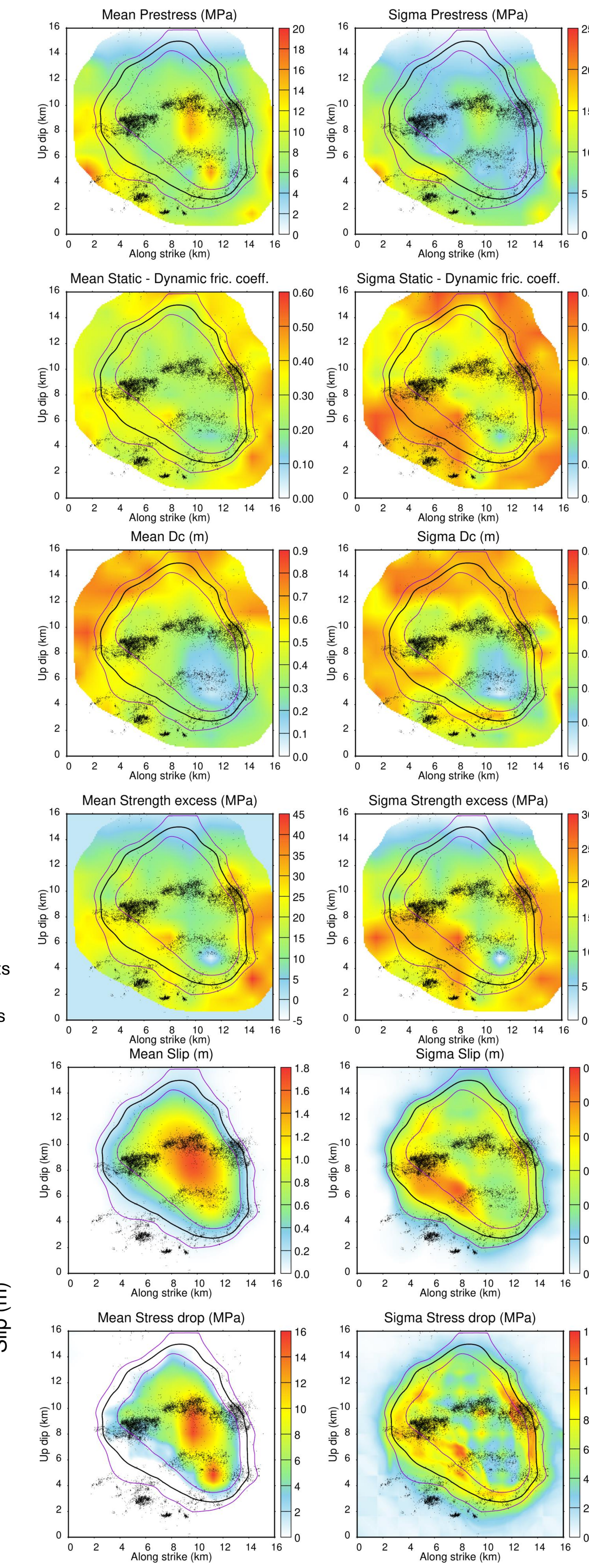

Figure 9: Mean input model parameters on the fault (averaged over the ensemble models) with their uncertainties in terms of one sigma interval, as inferred by the Bayesian dynamic finite fault inversion. Black and violet curves outline the contours of the mean slip model with one sigma uncertainties. Black dots denote the position of aftershocks and foreshocks.

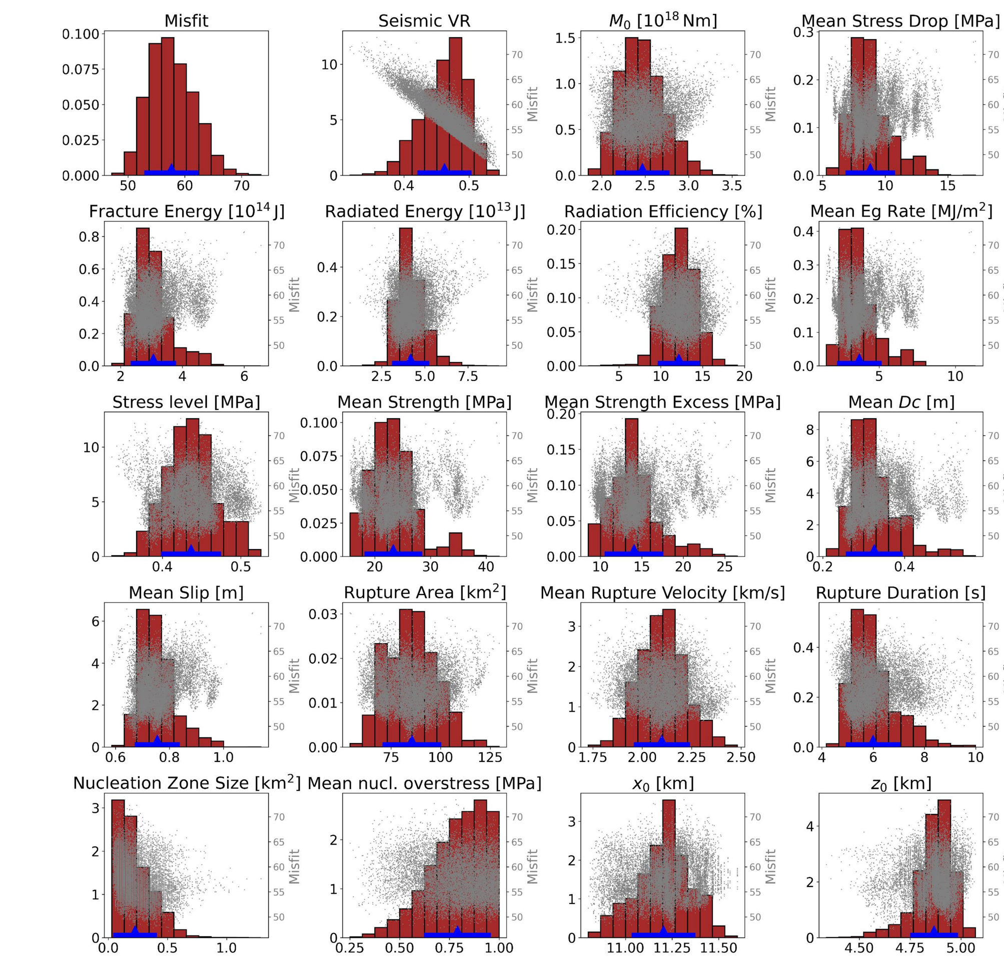

Figure 10: Normalized histograms of the kinematic and dynamic rupture parameters inverted by the Bayesian dynamic finite fault inversion. Gray dots denote the misfit values. Mean parameters are slip-averaged over the fault. Blue triangles and lines are the mean values over the ensembles with its one sigma (biased) standard deviation intervals, respectively.

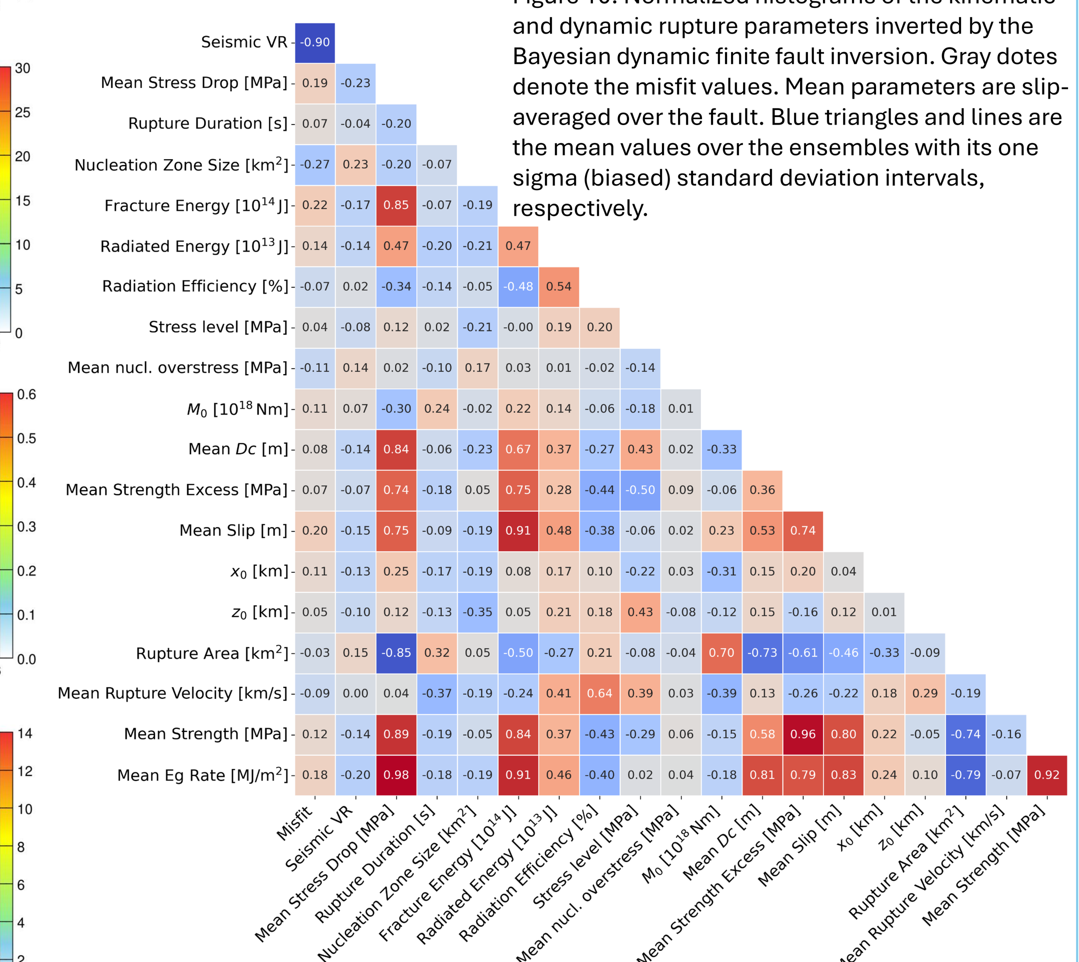

Figure 11: Correlation heatmap of inferred parameters. The numbers are the Pearson product-moment correlation coefficients. Mean parameters are slip-averaged.

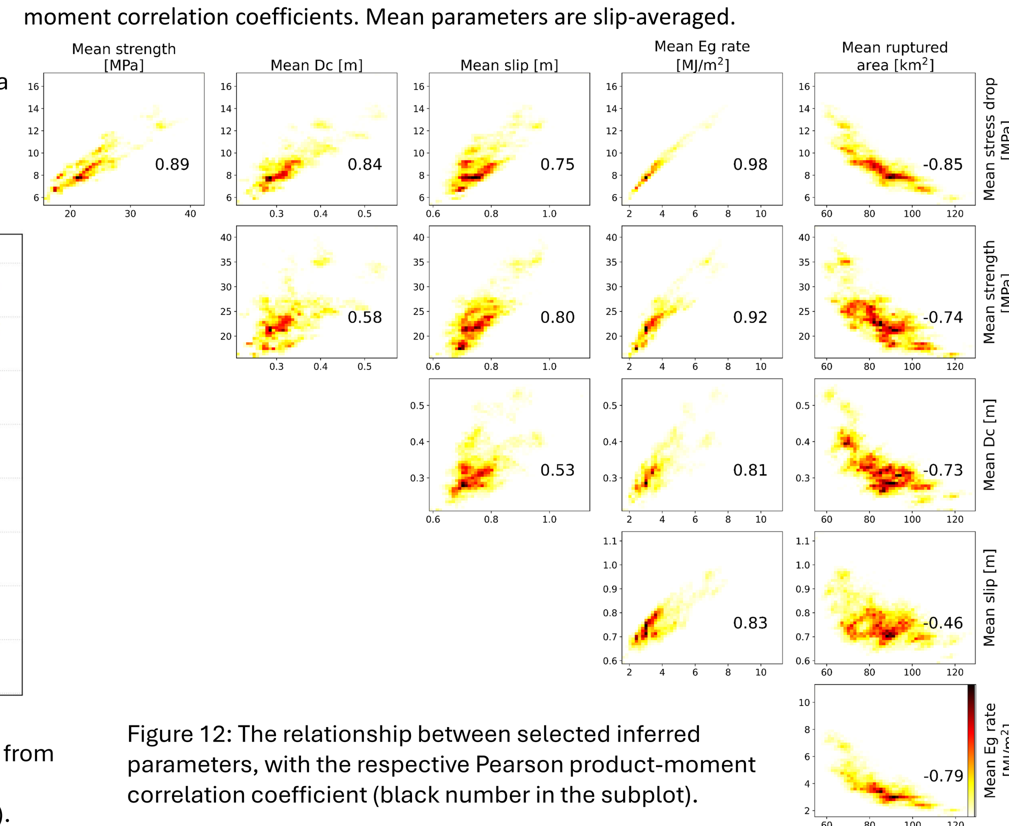

Figure 12: The relationship between selected inferred parameters, with the respective Pearson product-moment correlation coefficient (black number in the subplot).

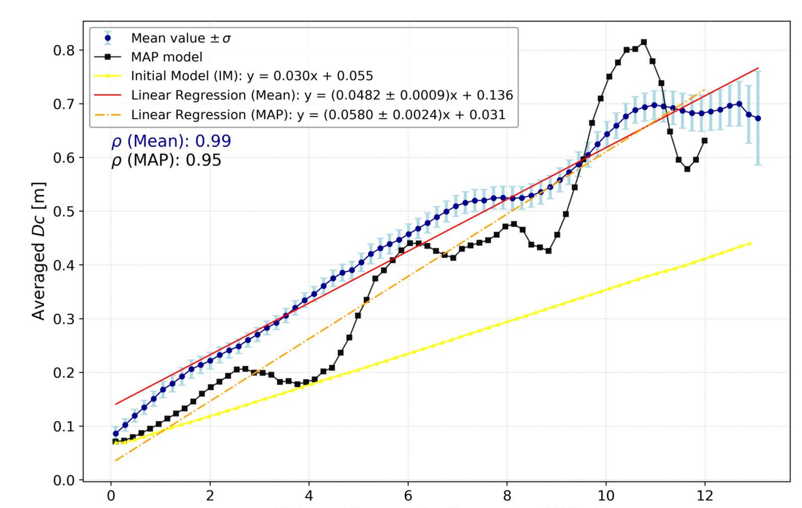

Figure 13: Averaged Dc values over the specified annulus of distance from nucleation center for the mean (blue), MAP (black) and initial model (yellow). The values are fitted with linear regression lines (see legend).

References:

- Aki K. and Richards P. G. Quantitative Seismology. University Science Books, 2 edition, 2002. ISBN 0935702962. URL.
- Amey R. M. J., Hooper A., & Morishita Y. (2019). Going to any lengths: Solving for fault size and fractal slip for the 2016, Mw 6.2 Central Tottori earthquake, Japan, using a transdimensional inversion scheme. Journal of Geophysical Research: Solid Earth, 124, 4001–4016. https://doi.org/10.1029/2018JB016434.
- Hisahiko Kubo, Wataru Suzuki, Shin Aoi, and Haruko Sekiguchi. Source rupture process of the 2016 central Tottori, Japan, earthquake (M JMA 6.6) inferred from strong motion waveforms. Earth, Planets and Space, 69, 12 2017. doi: 10.1186/s40623-017-0714-3.
- Gallovič F., Valentová Ľ., Ampuero J.-P., & Gabriel A.-A. (2019). Bayesian dynamic finite-fault inversion: 1. Method and synthetic test. Journal of Geophysical Research: Solid Earth, 124, 6949–6969. https://doi.org/10.1029/2019JB017510
- Gallovič F., Valentová Ľ., Ampuero J.-P., & Gabriel A.-A. (2019). Bayesian dynamic finite-fault inversion: 2. Application to the 2016 Mw 6.2 Amatrice, Italy, earthquake. Journal of Geophysical Research: Solid Earth, 124, 6970–6988. https://doi.org/10.1029/2019JB017512 .
- Koketsu, K.; Miyake, H., et al., 2012. An updated integrated velocity structure model of Japan based on recent geological and geophysical observations. Journal of Disaster Research. Available also from: https://www.iitk.ac.in/nicee/ publications.
- Meneses-Gutierrez A., Nishimura T., & Hashimoto M. (2019). Coseismic and postseismic deformation of the 2016 Central Tottori earthquake and its slip model. Journal of Geophysical Research: Solid Earth, 124, 2202–2217. https://doi.org/10.1029/2018JB016105.
- Premus J., Gallovič F., Hanyk L., and Gabriel A.-A. FD3D_TSN: A Fast and Simple Code for Dynamic Rupture Simulations with GPU Acceleration. Seismological Research Letters, 91(5):2881–2889, 06 2020. doi: 10.1785/0220190374.
- Sambridge, Malcolm, 2013. A Parallel Tempering algorithm for probabilistic sampling and multimodal optimization. Geophysical Journal International. Vol. 196, no. 1, pp. 357–374. issn 0956-540X. Available from doi: 10.1093/ gji/ggt342.
- Shibata, R., Aso, N., 2025. Kinematic Source Modeling Using Radiation-Corrected Empirical Green's Functions in Waveform Inversion. Bulletin of the Seismological Society of America. Available from doi: 10.1785/ 0120240077.
- Zachary R., Kanamori H., Hauksson E., and Aso N. Dissipative Intraplate Faulting During the 2016 Mw 6.2 Tottori, Japan Earthquake. Journal of Geophysical Research: Solid Earth, 123, 01 2018. doi: 10.1002/2017JB015077.